

Crystalline superconductor-semiconductor Josephson junctions for compact superconducting qubits

Jesse Balgley,^{1,*} Jinho Park,^{1,*} Xuanjing Chu,^{2,*} Ethan G. Arnault,³ Martin V. Gustafsson,⁴ Leonardo Ranzani,⁴ Madisen Holbrook,⁵ Kenji Watanabe,⁶ Takashi Taniguchi,⁶ Vasili Perebeinos,⁷ James Hone,¹ and Kin Chung Fong^{4,†}

¹*Department of Mechanical Engineering, Columbia University, New York, NY 10027, USA*

²*Department of Applied Physics and Mathematics, Columbia University, New York, NY 10027, USA*

³*Department of Electrical Engineering and Computer Science,
Massachusetts Institute of Technology, Cambridge, MA 02139*

⁴*RTX BBN Technologies, Quantum Engineering and Computing Group, Cambridge, MA 02138, USA*

⁵*Department of Physics, Columbia University, New York, NY 10027, USA*

⁶*National Institute for Materials Science, 1-2-1 Sengen, Tsukuba, Ibaraki 305-0044, Japan*

⁷*Department of Electrical Engineering, University at Buffalo,
The State University of New York, Buffalo, New York 14260, USA*

(Dated: January 28, 2025)

The narrow bandgap of semiconductors allows for thick, uniform Josephson junction barriers, potentially enabling reproducible, stable, and compact superconducting qubits. We study vertically stacked van der Waals Josephson junctions with semiconducting weak links, whose crystalline structures and clean interfaces offer a promising platform for quantum devices. We observe robust Josephson coupling across 2–12 nm (3–18 atomic layers) of semiconducting WSe₂ and, notably, a crossover from proximity- to tunneling-type behavior with increasing weak link thickness. Building on these results, we fabricate a prototype all-crystalline merged-element transmon qubit with transmon frequency and anharmonicity closely matching design parameters. We demonstrate dispersive coupling between this transmon and a microwave resonator, highlighting the potential of crystalline superconductor-semiconductor structures for compact, tailored superconducting quantum devices.

State-of-the-art transmon qubits rely on Josephson junctions (JJs) with amorphous insulating weak links. However, their large bandgaps necessitate extremely thin barriers, compromising uniformity, reproducibility, and precise control of junction critical current which controls qubit frequency and charge sensitivity. Pinholes and grain boundaries in these materials further constrain JJ sizes, and transmons based on such JJs typically require large footprint shunt capacitors for ideal transmon capacitances [1].

In contrast, semiconducting weak links offer precise control of junction properties over a wide range [2], and their reduced bandgaps allow for thicker barriers, which are less prone to pinhole formation compared to typical insulating barriers [3]. This enables larger-area JJs with built-in capacitance, forming a smaller-footprint “merged-element” transmon (MET) [4]. Recent advances in vertical JJs with semiconducting weak links have achieved fine control of junction critical current over a wide range [5] but relied on amorphous barriers that host high densities of microwave-active two-level systems, a primary factor limiting superconducting qubits lifetimes [6].

Crystalline materials, characterized by their lack of grain boundaries, atomically pristine interfaces, and reduced two-level fluctuator densities [7], offer a promising alternative platform for high-quality quantum devices. Beyond epitaxial crystalline materials [8–10], layered van der Waals (vdW) materials, which can be peeled apart into atomically thin layers, present distinctive features to create low-loss and novel devices [11, 12]. For example, they may be readily encapsulated as protection against oxidation, and can be “stacked” together in complex *heterostructures* of different vdW materials [13] with highly ordered internal interfaces [14]. Their layered structure facilitates unprecedented uniformity and reproducibility compared to deposited thin films. To date, however, studies

of vdW JJs have primarily focused either on vertical junctions incorporating weak links ≤ 6 vdW layers thick [15–20], or on lateral junctions with monolayer vdW weak links [21–25].

In this manuscript, we systematically investigate DC electronic transport in vertical vdW JJs with semiconducting weak links in the 2–12 nm thickness range, aimed at advancing a materials platform for transmon qubits. As we vary the thickness of the semiconductor, we observe a crossover from proximity-type to tunneling-type behavior around 7 atomic layers. These findings inform the optimal semiconductor weak link thicknesses for compact METs. As a proof of concept, we fabricate a prototype all-vdW MET and demonstrate its operation as a two-level system via dispersive readout.

We study vertical crystalline JJs consisting of NbSe₂, an anisotropic *s*-wave vdW superconductor (critical temperature 7.2 K, superconducting gap 1.3 meV [26]), sandwiching WSe₂, a vdW semiconductor with a 1.2 eV indirect bulk bandgap [27]. This is ~ 6 times smaller than the bandgap of aluminum oxide and ~ 5 times smaller than that of the vdW insulator hexagonal boron nitride (hBN), which acts as a tunnel barrier even in the single-layer limit [28]. The lower tunnel barrier height in WSe₂ allows for a thicker, more uniform weak link. Consequently, the junction critical current can be controlled in small increments by changing the number of vdW layers in the WSe₂ weak link. We exfoliate flakes of WSe₂ and NbSe₂ from bulk crystals and build stacks with them after identifying flakes with suitable geometries (see Supplemental Material). We encapsulate the JJs in flakes of hBN to protect them from surface contamination and oxidation (Fig. 1(a)).

In total, we study DC electronic transport in twenty JJs with WSe₂ thicknesses ranging from 3 to 18 layers. An example *I*-*V* curve of a JJ with a 9-layer-thick WSe₂ weak link taken at temperature $T = 20$ mK is shown in Fig. 1(b). Sweeps of

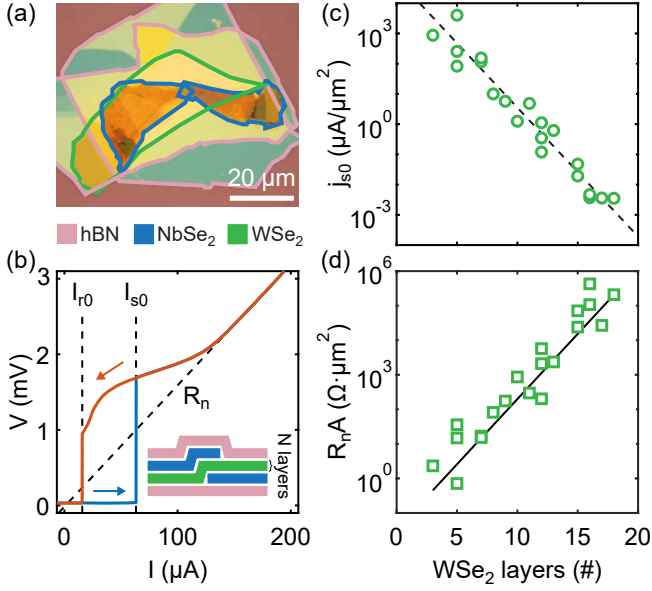


FIG. 1. Josephson junction characterization. (a) Optical image of an NbSe₂/WSe₂/NbSe₂ JJ encapsulated in hBN flakes. (b), I - V curve for a JJ with a 9-layer-thick WSe₂ weak link, with dashed lines marking how I_s , I_r , and R_n are obtained. Blue (red) trace indicates increasing (decreasing) bias current sweep. Inset, schematic of a vdW JJ. (c), Switching current density at $T = 20$ mK, j_{s0} , and (d), normal-state-resistance-area product, $R_n A$, as functions of WSe₂ weak link thickness. The black dashed line in (c) is an exponential fit to the data to guide the eye. The solid black line in (d) results from the resistivity simulations within the Thomas-Fermi model.

increasing (blue trace) and decreasing (red trace) bias current allow us to extract key JJ parameters: the switching current I_{s0} , the retrapping current I_{r0} , and the normal state resistance R_n . The subscript “0” indicates values at $T = 20$ mK. In Fig. 1(c) & (d) we plot the switching current density $j_{s0} = I_{s0}/A$ and the product of the normal state resistance and JJ area, $R_n A$, respectively. A defined by the overlapping area of the two NbSe₂ flakes sandwiching the WSe₂ weak link. Both j_{s0} and $R_n A$ obey exponential dependencies over roughly six orders of magnitude as a function of the WSe₂ thickness. The trends in these quantities are robust despite some scatter in the data, which we attribute to uncertainty in the JJ geometry (see Supplemental Material). As we will show, the trend of j_{s0} versus WSe₂ thickness enables accurate prediction of the $0 \rightarrow 1$ frequency of a transmon qubit.

To illustrate the impact of the semiconductor weak link thickness on the electronic properties of vertical JJs, in Fig. 2(a) & (b) we plot example DC I - V transport characteristics of current-biased junctions with 7-layer-thick (7L) and 13-layer-thick (13L) WSe₂ weak links, respectively. Blue (red) traces indicate increasing (decreasing) bias current, all taken at $T = 20$ mK. In the 13L device, the retrapping current ($I_{r0} = 0.2$ μ A) is two orders of magnitude smaller than the switching current ($I_{s0} = 24$ μ A), whereas those of 7L (574 μ A and 830 μ A, respectively) are within a factor of two of each

other [29]. The ratio I_{s0}/I_{r0} provides a measure of the JJ I - V hysteresis, which we plot for all devices in Fig. 2(c). In the range of 3–7 layers, I_{s0}/I_{r0} is saturated around 1. Above 7 layers, the hysteresis increases exponentially with WSe₂ thickness. $I_{s0}/I_{r0} \approx 1$ corresponds to minimal hysteresis typical of proximity-type JJs [30]. Though proximity JJs possess a conductive weak link between the superconducting electrodes, which in principle should yield a nonhysteretic I - V , finite circuit capacitances and Joule heating in the normal state can contribute to finite hysteresis [30]. On the other hand, pronounced hysteresis is characteristic of tunneling-type JJs with insulating weak links [31, 32]. These two different hysteretic behaviors suggest that there is a crossover from proximity- to tunneling-type JJ as the WSe₂ thickness increases.

Further evidence of such a crossover is provided by the temperature dependence of the switching and retrapping currents, measured in fourteen devices with WSe₂ thicknesses ranging from 3 to 13 layers. In Fig. 3(a), we plot the temperature-dependent switching current I_s (which we use as a proxy for the critical current I_c), multiplied by R_n . The solid black line represents the Ambegaokar-Baratoff (A-B) limit of an ideal tunnel junction: $I_c R_n = (\pi/2)\Delta \tanh[\Delta/2k_B T]/e$ [33]. Here, Δ is the superconducting gap at temperature T , for which we use the BCS interpolation formula $\Delta = \Delta_0 \tanh[(\pi k_B T_c / \Delta_0) \sqrt{T_c/T - 1}]$ [34]. $\Delta_0 = 1.764 k_B T_c \approx 1$ meV is the zero-temperature gap value proportional to the junction critical temperature $T_c = 6.8$ K. Systematically, we find that the $I_s R_n$ products of all junctions with weak link thicknesses ≤ 7 layers (light to dark blue circles) exceed the A-B limit, whereas those with weak links > 7 -layers thick (yellow to red circles) undershoot the predicted value. The $I_c R_n$ product of a JJ exceeds the A-B limit when the transparency of the weak link is finite, *i.e.*, in a proximity-type junction [35–37]. On the other hand, $I_c R_n$ in a JJ with an ideal tunnel barrier should correspond precisely to the A-B limit. However, superconducting proximity effects or a finite boundary resistance at the superconductor-weak link interface can lead to a reduction in $I_c R_n$ to a value below the A-B limit [38–40]. The grouping of $I_s R_n$ above and below the A-B limit around 7 layers of WSe₂ again suggests either proximity- or tunneling-type behavior occurs, depending on the WSe₂ thickness.

We corroborate the crossover between two Josephson junction regimes by investigating the temperature-dependent retrapping current, plotted in Fig. 3(b) normalized by the base-temperature switching current as I_r/I_{s0} . In JJs with WSe₂ weak links thinner than 8 layers (light to dark blue circles) I_r/I_{s0} monotonically decreases with increasing temperature. For ≥ 8 -layer-thick WSe₂ (yellow to red circles) I_r/I_{s0} is non-monotonic, wherein the retrapping current, constant at low temperatures, first rises as the temperature increases before eventually decreasing for temperatures above 5 K.

We may understand the nonmonotonic temperature dependence of the retrapping current in tunneling-type JJs by recalling that the current-voltage relation of a JJ is related to the evolution of the difference in the phases of the order parameter between the two superconductors. In the resistively

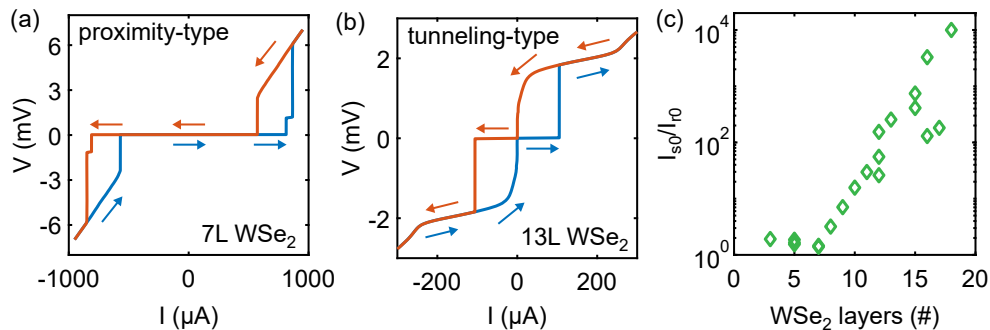


FIG. 2. Hysteresis in a vertical superconductor-semiconductor Josephson junction. (a,b), DC I - V curves for current-biased JJs with 7-layer-thick and 13-layer-thick WSe_2 weak links, respectively. Blue (red) traces indicate sweeps from negative to positive (positive to negative) current bias. (c), I_{s0}/I_{r0} as a function of WSe_2 weak link thickness.

and capacitively shunted junction (RCSJ) model [31, 32], the current-biased junction is modeled as a parallel combination of an ideal Josephson element, a capacitor, and a resistor, and the phase difference across the junction behaves as a particle subject to a tilted washboard potential. The damping of the motion of this “phase particle” is inversely proportional to the junction resistance [31, 32]. In a tunneling-type JJ with low damping (high junction resistance), the particle can escape from the potential well when the current bias is increased, leading to a transition from the zero-voltage state to the resistive state. However, due to its inertia, the particle may not retrap back into the zero-voltage state unless the current is reduced significantly, creating hysteresis. At low temperatures, the damping is constant and the tunnel junction exhibits pronounced

hysteresis. According to the quasiparticle tunneling model of Chen, Fisher, & Leggett [41], as the temperature increases, thermal excitation facilitates quasiparticle tunneling across the junction, increasing the effective damping. This increases the retrapping current and reduces the hysteresis. Close to the critical temperature, the superconducting gap diminishes substantially, reducing both the critical and retrapping currents. This process explains the qualitative behavior of I_r/I_{s0} in JJs with WSe_2 thickness ≥ 8 layers. In contrast, in proximity-type JJs where the weak link can readily conduct quasiparticles between the superconducting electrodes, the change in damping due to thermal activation of quasiparticles is negligible. Thus, the retrapping current in proximity-type JJs has a monotonic trend as a function of temperature, as seen for WSe_2 weak links thinner than 8 layers.

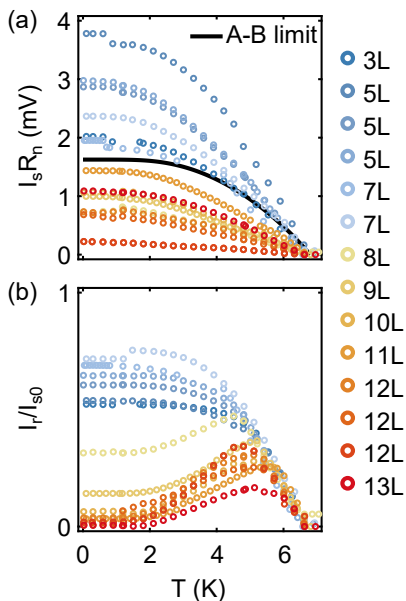


FIG. 3. Temperature dependence of Josephson junction properties. (a), Temperature dependence of $I_s R_n$. (b), Temperature dependence of retrapping current I_r normalized by I_{s0} .

In $\text{NbSe}_2/\text{WSe}_2/\text{NbSe}_2$ JJs, a crossover from proximity-type to tunneling-type behavior with weak link thickness is plausible if we consider the relative band alignment between the two materials. *Ab initio* calculations estimate a work function mismatch of ≈ 1.3 eV between the two materials, with the Fermi energy of NbSe_2 intersecting the valence band of WSe_2 [42]. Such a work function mismatch leads to an interfacial charge transfer between the two materials [43, 44], which can form an accumulation region of hole-doped WSe_2 . When the WSe_2 weak link is thinner than the accumulation regions formed by each NbSe_2 electrode, the entire weak link will be doped and conductive, forming a proximity-type JJ. When the WSe_2 is thicker than the accumulation regions, the central layers will remain undoped, providing a tunnel barrier for the JJ. In the superconducting state, we infer from the data that ≈ 3 layers (2 nm) of WSe_2 are doped by each NbSe_2 electrode, leading to proximity-type behavior in JJs with WSe_2 weak links thinner than 7 layers, and tunneling-type behavior when the WSe_2 is thicker than 7 layers. The work function mismatch between the two materials also dictates the strength of the exponential dependence of j_{s0} and $R_n A$ on weak link thickness. We employ the Thomas-Fermi model to calculate the normal state resistance for this material system, the result of which is shown in Fig. 1(d) (see Supplemental Material for details). The slope

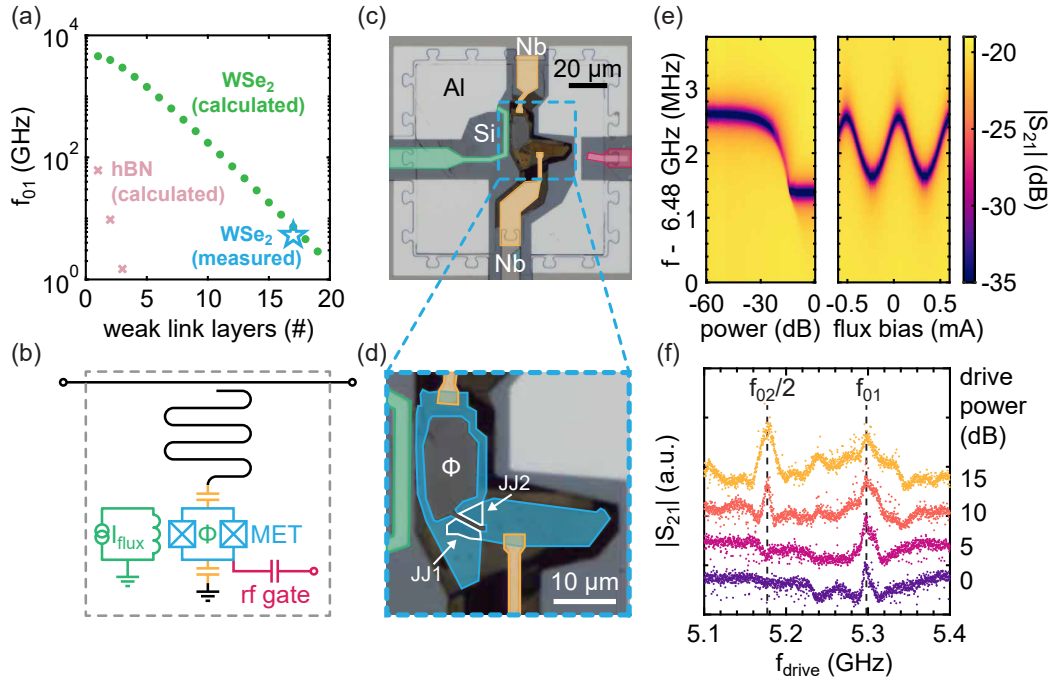


FIG. 4. van der Waals merged-element transmon. (a) Calculated MET $0 \rightarrow 1$ transition frequency f_{01} for varying numbers of WSe₂ (green circles) and hBN (pink crosses) weak links, and the measured f_{01} (blue star) for the MET shown in (c). (b), MET circuit schematic. (c), Optical image of a vdW MET. Capacitive coupling wires, flux bias line, and rf drive line are false-colored orange, green, & red, respectively. (d), Zoom-in of the vdW stack in (c) showing the SQUID flux loop shaded blue with two JJ areas outlined in white. (e), Single-tone spectroscopy as a function of readout power (left) and flux bias current at low microwave power (right). (f), Two-tone spectroscopy. Drive pulse power increases from purple to violet to pink to gold traces, which are vertically offset for clarity.

of the resistance in the semi-logarithmic plot of Fig. 1(d) is determined by the Fermi level position inside the tunnel junction, which we determine to be 28.4 meV above the valence band of WSe₂ based on the fit to the data. Considering the individual material properties and work function mismatch, we find quantitative agreement between the measured and calculated tunneling resistance in NbSe₂/WSe₂/NbSe₂ JJs.

Having characterized the effects of semiconducting weak link thickness on the properties of a vdW JJ, we predict the properties of an NbSe₂/WSe₂/NbSe₂-based MET to determine what weak link thicknesses will result in a qubit $0 \rightarrow 1$ transition frequency f_{01} in the range of 1–15 GHz with sufficient anharmonicity between subsequent qubit energy levels. Using the exponential fit of j_{s0} from Fig. 1(c) and the expected geometric junction parallel-plate capacitance, we calculate the expected MET frequencies of JJs with 1–20 layers of WSe₂ weak link (Fig. 4(a)). Here, we use $f_{01} = (\sqrt{8E_J E_C} - E_C)/h$, where h is Planck’s constant, $E_J = \Phi_0 I_c / 2\pi$ is the Josephson energy with $\Phi_0 = h/2e$ the superconducting flux quantum, e the elementary charge, and $E_C = e^2/2C$ the charging energy [1]. For comparison, we plot the calculated f_{01} for JJs with hBN weak links using previously measured tunneling resistance values [28] and the Ambegaokar-Baratoff relation to estimate the critical current. Compared to WSe₂, hBN shows much coarser variation in f_{01} with layer number due to its large bandgap, increasing by roughly an order of magnitude

with each added vdW layer and requiring extremely thin weak links which are difficult to isolate and construct JJs with. In contrast, we find that JJs with 15–20-layer-thick WSe₂ weak links can produce METs with frequencies between 1–15 GHz.

To test these predictions, we fabricate a prototype all-vdW-material MET, comprising an NbSe₂/17-layer-thick WSe₂/NbSe₂ JJ. The MET readout circuit, depicted schematically in Fig. 4(b), consists of a hanger-type microwave readout resonator capacitively coupled on one end to a microwave feedline with characteristic impedance $Z_0 = 50 \Omega$. The JJ is fashioned into a SQUID loop using reactive ion etching in a lithographically defined window and is capacitively coupled to the readout resonator at one end, and to ground at the other, by lithographically defined leads. We include additional flux bias and microwave drive lines for tuning and control. Fig. 4(c) shows an optical image of the vdW MET, magnified in Fig. 4(d).

In this device, we confirm dispersive interaction between the readout resonator and the MET by measuring the transmission coefficient S_{21} of the feedline near the readout resonator frequency as a function of power and flux bias current (Fig. 4(e)). We observe a distinct shift in resonator frequency below a critical power level, indicating the onset of dispersive coupling to a two-level system. In the low-power regime, the resonator frequency shows a periodic response to magnetic flux threaded through the SQUID loop, affirming that

it is interacting with the frequency-tunable vdW SQUID. In Fig. 4(f), we plot two-tone spectroscopy of the device taken at the flux-bias “sweet spot” where the change in the readout resonator frequency versus flux is minimized. Here, we input to the feedline a continuous weak probe tone near the readout resonator center frequency, as well as a microwave pulse at frequency f_{drive} , intended to create excitations in the two-level system. We record the change in $|S_{21}|$ at the probe frequency that results as we vary the f_{drive} and the drive amplitude. At low amplitudes (purple data), we observe a sharp peak in the response at $f_{\text{drive}} \approx 5.30$ GHz, which we identify as f_{01} . As we increase the drive amplitude (purple to violet to pink to gold) the peak at f_{01} broadens while a second peak at ≈ 5.18 GHz emerges. We designate this to be $f_{02}/2$, half the $0 \rightarrow 2$ transition frequency, emerging as the result of a two-photon excitation process. From this, we obtain the transmon anharmonicity $\alpha = f_{21} - f_{01} = -242$ MHz. We calculate $E_J/E_C = 66$ for this qubit, placing it well within the transmon regime [1]. The measured f_{01} is within 10% of the expected value, validating that the DC transport characterization of vdW JJs with semiconducting weak links can be used to accurately design transmon qubits.

In summary, we have studied DC electronic transport in crystalline vertical Josephson junctions made of superconducting NbSe₂ and semiconducting WSe₂ weak links with thicknesses varying from 3–18 vdW layers. Trends in the junction switching current, retrapping current, and hysteresis as functions of WSe₂ thickness and temperature reveal a crossover from proximity-type to tunneling-type junction behavior around 7 layers of WSe₂. We attribute this crossover to the work function mismatch between the superconductor and semiconductor, underscoring the importance of the choice of materials used in superconductor-semiconductor quantum devices. Using the exponential dependence of the JJ critical current density on weak link thickness, we calculated the frequencies of merged-element transmon qubits based on these crystalline JJs and validated the accuracy of these predictions by fabricating a prototype all-crystalline-material-based MET. Importantly, these qubits offer a remarkably small footprint with qubit transition frequencies that can range from a few GHz to millimeter-wave frequencies [45]. Our results support that crystalline superconductor-semiconductor JJs are a promising platform for compact superconducting qubits with distinctive design flexibility and tunability.

Acknowledgements—This work was primarily supported by the Army Research Office under Contract W911NF-22-C-0021 (NextNEQST SuperVan-2). Synthesis and characterization of WSe₂ crystals (M.H.) and the use of facilities and instrumentation for sample assembly (J.B.) were supported by National Science Foundation through the Columbia University, Columbia Nano Initiative, and the Materials Research Science and Engineering Center (DMR-2011738). Theoretical modeling (V.P.) was supported by the National Science Foundation (Grant No. 2235276). Synthesis of boron nitride (K.W. and T.T.) was supported by the Elemental Strategy Initiative conducted by the MEXT, Japan

(Grant No. JPMXP0112101001) and JSPS KAKENHI (Grant Nos. JP19H05790 and JP20H00354). J.H. acknowledges support from the Gordon and Betty Moore Foundation’s EPiQS Initiative, Grant GBMF10277. J.P. acknowledges support from the education and training program of the Quantum Information Research Support Center, funded through the National Research Foundation of Korea (NRF) by the Ministry of Science and ICT (MSIT) of the Korean government (No. 2021M3H3A1036573).

SUPPLEMENTAL MATERIAL

Methods

WSe₂ crystals are synthesized using the two-step flux synthesis method [46]. We mechanically exfoliate hBN and WSe₂ flakes from bulk crystals in air and use atomic force microscopy (AFM) to scan flakes for cleanliness and determine their thickness. While AFM is a sensitive and commonly used probe of vdW materials, the presence of physisorbed organic molecules or water on or under exfoliated flakes, air gaps, or instrumental offset can impede the accurate determination of vdW flake thickness using atomic force microscopy. This leads to a typical uncertainty of around ± 1 atomic layer [47] for our WSe₂ flakes. Other techniques to determine thickness like second harmonic generation may be used in future works to more accurately determine the layer number [48].

NbSe₂ flake exfoliation and vdW device stacking are performed in a glovebox under a N₂-rich atmosphere (< 0.5 ppm O₂ & H₂O) to minimize oxidation during fabrication. During stacking, bubbles which commonly form in vdW heterostructures can lead to further uncertainty in the Josephson junction geometry, as the effective junction area defined by the overlap of the two NbSe₂ electrodes may be reduced by the presence of bubbles. We use an MMA/PMMA bilayer resist for e-beam lithography. CF₄ reactive ion etching is performed to modify the device area, and CHF₃ etching is used to etch regions of the encapsulating hBN and expose NbSe₂ for electrical contact. Before metal deposition, oxidized surface NbSe₂ layers are removed *in situ* using argon ion-milling. Then, we deposit 3-nm-thick titanium sticking layer and 40–60 nm aluminum leads by e-beam evaporation in the same chamber [11].

We characterize our NbSe₂/WSe₂/NbSe₂ Josephson junctions (JJs) using 4-terminal DC transport measurements in a dilution refrigerator with a base temperature below 20 mK. The bias current is swept through the junctions while the voltage difference across them is measured. This bias current is applied through a load resistor, whose resistance is much greater than the junction resistance, in series with a voltage source. The voltage across the junction is amplified and then read by a digital multimeter. To prevent high-frequency noise from exciting the junctions, a two-stage low-pass filter with a cutoff frequency of approximately 20 kHz is installed on all DC lines at the 4 K stage. All measurements are performed after stabilizing the temperature for at least 20 minutes.

MET devices are mounted on the cold finger of a dilution refrigerator with a base temperature below 20 mK. To reduce decoherence from external magnetic fields, the cold finger is enclosed in Cryoperm magnetic shielding. On the input side, the total line attenuation ranges from 70 dB to 84 dB, depending on the resonance frequency, with a 40 dB attenuator placed on the mixing chamber to further protect the qubit from thermal radiation. On the output side, a circulator is installed to block noise from external sources and prevent the input signal from reflecting back into the qubit. The output signal is amplified by low-temperature and room-temperature amplifiers. The qubit transition of the MET device, as shown in Fig. 4(f) of the main text, is characterized using a two-tone pulse measurement. A fixed DC current of 55 μA is applied to generate magnetic flux, positioning the transmon at its least susceptible point to flux noise. Both the cavity readout and qubit control pulses are fed through the transmission line's input port.

Thomas-Fermi Model for Self-Consistent Potential in the Tunneling Region

We employ the Thomas-Fermi model to simulate charge carrier density in layers of WSe₂ between NbSe₂ electrodes by solving the Poisson equation for the self-consistent potential $V(x)$:

$$\epsilon \frac{d^2 V(x)}{dx^2} = -\rho(x) \quad (1)$$

where $\epsilon = 6.4$ is the dielectric constant in the perpendicular to the of WSe₂ plane direction. The charge carrier density $\rho(x)$ is found from the 2D carrier density on each WSe₂ layer n_i separated by distance $d = 6.5 \text{ \AA}$:

$$\rho(x) = \sum_{i=1}^N n_i \exp\left(-\frac{(x - d \cdot i)^2}{\sigma^2}\right) / (\sqrt{\pi} \sigma) \quad (2)$$

where we employ Gaussian broadening with $\sigma = 3 \text{ \AA}$ to mimic the finite width of the electron cloud between WSe₂ layers. The 2D charge carrier density n_i depends on the electrostatic potential $V_i = V(d \cdot i)$ in the middle of the monolayers, which is found self-consistently:

$$n_i(V_i) = kT \cdot \frac{2m_h}{\pi \hbar^2} \cdot \ln\left(\frac{1 + e^{-\frac{eV_i + \Delta W}{kT}}}{1 + e^{-\frac{eV_i - E_g - \Delta W}{kT}}}\right) \quad (3)$$

where $m_h = 0.6 m_e$ is the hole effective mass in WSe₂ in units of electron mass m_e , $\Delta W = 1.3 \text{ eV}$ [42] is the workfunction mismatch between NbSe₂ and WSe₂, and E_g is the bandgap of WSe₂. We choose the Fermi energy in the metal as zero of energy and the boundary condition of $V(x=0) = V(x=L) = 0 \text{ V}$, where $L = d \cdot (N + 1)$, imply hole doping of WSe₂ near the contacts.

Once the self-consistent potential $V(x)$ is obtained for junctions with different numbers of layer N , we use WKB approximation to calculate tunneling conductance according to:

$$G = G_M \int_{-\infty}^{+\infty} T(E) \left(-\frac{\partial f(E, E_F, T)}{\partial E}\right) dE, \\ T(E) = \exp\left(-2 \int_0^L \sqrt{\frac{2m_h(E - eV(x) - \Delta W)}{\hbar^2}} dx\right) \quad (4)$$

where $G_M = 5.6 \text{ S}\mu\text{m}^{-2}$ is a single parameter fit which has the meaning of a product of ballistic conductance of NbSe₂ and an additional scattering barrier at the NbSe₂/WSe₂ interface due to the wavefunction mismatch in two materials. The resulting resistance $1/G$ simulated at $T \rightarrow 0 \text{ K}$ limit is plotted in Fig. 1(d) in the main text.

* These authors contributed equally to this work.

† Present address: k.fong@northeastern.edu, Northeastern University

- [1] J. Koch, T. M. Yu, J. Gambetta, A. A. Houck, D. I. Schuster, J. Majer, A. Blais, M. H. Devoret, S. M. Girvin, and R. J. Schoelkopf, *Physical Review A* **76**, 042319 (2007).
- [2] Y.-P. Shim and C. Tahan, *Nature Communications* **5**, 4225 (2014).
- [3] D. Willsch, D. Rieger, P. Winkel, M. Willsch, C. Dickel, J. Krause, Y. Ando, R. Lescanne, Z. Leghtas, N. T. Bronn, P. Deb, O. Lanes, Z. K. Mineev, B. Dennig, S. Geisert, S. Günzler, S. Ihssen, P. Paluch, T. Reisinger, R. Hanna, J. H. Bae, P. Schüffelgen, D. Grützmacher, L. Buimaga-Iarinca, C. Morari, W. Wernsdorfer, D. P. DiVincenzo, K. Michielsen, G. Catelani, and I. M. Pop, *Nature Physics* **20**, 815 (2024).
- [4] R. Zhao, S. Park, T. Zhao, M. Bal, C. McRae, J. Long, and D. Pappas, *Physical Review Applied* **14**, 064006 (2020).
- [5] D. I. Olaya, J. Biesecker, M. A. Castellanos-Beltran, A. J. Sirois, P. F. Hopkins, P. D. Dresselhaus, and S. P. Benz, *Applied Physics Letters* **122** (2023).
- [6] N. P. de Leon, K. M. Itoh, D. Kim, K. K. Mehta, T. E. Northup, H. Paik, B. S. Palmer, N. Samarth, S. Sangtawesin, and D. W. Steuerman, *Science* **372** (2021).
- [7] S. Oh, K. Cicak, J. S. Kline, M. A. Sillanpää, K. D. Osborn, J. D. Whittaker, R. W. Simmonds, and D. P. Pappas, *Physical Review B* **74**, 100502 (2006).
- [8] J. Shabani, M. Kjaergaard, H. J. Suominen, Y. Kim, F. Nichele, K. Pakrouski, T. Stankevic, R. M. Lutchyn, P. Krogstrup, R. Feidenhans'l, S. Kraemer, C. Nayak, M. Troyer, C. M. Marcus, and C. J. Palmström, *Physical Review B* **93**, 155402 (2016).
- [9] C. J. K. Richardson, A. Alexander, C. G. Weddle, B. Arey, and M. Olszta, *Journal of Applied Physics* **127** (2020).
- [10] A. Goswami, A. P. McFadden, T. Zhao, H. Inbar, J. T. Dong, R. Zhao, C. R. H. McRae, R. W. Simmonds, C. J. Palmström, and D. P. Pappas, *Applied Physics Letters* **121** (2022).
- [11] A. Antony, M. V. Gustafsson, A. Rajendran, A. Benyamini, G. Ribeill, T. A. Ohki, J. Hone, and K. C. Fong, *Journal of Physics: Condensed Matter* **34**, 103001 (2022).
- [12] J. I. Wang, M. A. Yamoah, Q. Li, A. H. Karamlou, T. Dinh, B. Kannan, J. Braumüller, D. Kim, A. J. Melville, S. E. Muschinske, B. M. Niedzielski, K. Serniak, Y. Sung, R. Winik, J. L. Yoder, M. E. Schwartz, K. Watanabe, T. Taniguchi, T. P.

- Orlando, S. Gustavsson, P. Jarillo-Herrero, and W. D. Oliver, *Nature Materials* **21**, 398 (2022).
- [13] L. Wang, I. Meric, P. Y. Huang, Q. Gao, Y. Gao, H. Tran, T. Taniguchi, K. Watanabe, L. M. Campos, D. A. Muller, J. Guo, P. Kim, J. Hone, K. L. Shepard, and C. R. Dean, *Science* **342**, 614 (2013).
- [14] C. R. Dean, L. Wang, P. Maher, C. Forsythe, F. Ghahari, Y. Gao, J. Katoch, M. Ishigami, P. Moon, M. Koshino, T. Taniguchi, K. Watanabe, K. L. Shepard, J. Hone, and P. Kim, *Nature*, **1** (2012).
- [15] G. H. Lee, S. Kim, S. H. Jhi, and H. J. Lee, *Nature Communications* **6** (2015).
- [16] J. O. Island, G. A. Steele, H. S. J. van der Zant, and A. Castellanos-Gomez, *2D Materials* **3**, 031002 (2016).
- [17] M. Kim, G.-H. Park, J. Lee, J. H. Lee, J. Park, H. Lee, G.-H. Lee, and H.-J. Lee, *Nano Letters* **17**, 6125 (2017).
- [18] K. H. Lee, S. Chakram, S. E. Kim, F. Mujid, A. Ray, H. Gao, C. Park, Y. Zhong, D. A. Muller, D. I. Schuster, and J. Park, *Nano Letters* **19**, 8287 (2019).
- [19] C. Boix-Constant, S. Mañas-Valero, R. Córdoba, and E. Coronado, *Advanced Electronic Materials* **7**, 2000987 (2021).
- [20] J. Tian, L. A. Jauregui, C. D. Wilen, A. F. Rigosi, D. B. Newell, R. McDermott, and Y. P. Chen, *Journal of Physics: Condensed Matter* **33**, 495301 (2021).
- [21] X. Du, I. Skachko, and E. Y. Andrei, *Physical Review B* **77**, 184507 (2008).
- [22] F. Miao, W. Bao, H. Zhang, and C. N. Lau, *Solid State Communications* **149**, 1046 (2009).
- [23] G. H. Lee, D. Jeong, J. H. Choi, Y. J. Doh, and H. J. Lee, *Physical Review Letters* **107**, 1 (2011).
- [24] M. Ohtomo, R. S. Deacon, M. Hosoda, N. Fushimi, H. Hosoi, M. D. Randle, M. Ohfuchi, K. Kawaguchi, K. Ishibashi, and S. Sato, *Applied Physics Express* **15**, 075003 (2022).
- [25] M. Endres, A. Kononov, H. S. Arachchige, J. Yan, D. Mandrus, K. Watanabe, T. Taniguchi, and C. Schönenberger, *Nano Letters* **23**, 4654 (2023).
- [26] I. Guillaumon, H. Suderow, F. Guinea, and S. Vieira, *Physical Review B* **77**, 134505 (2008).
- [27] K. K. Kam and B. A. Parkinson, *The Journal of Physical Chemistry* **86**, 463 (1982).
- [28] L. Britnell, R. V. Gorbachev, R. Jalil, B. D. Belle, F. Schedin, M. I. Katsnelson, L. Eaves, S. V. Morozov, A. S. Mayorov, N. M. R. Peres, A. H. Castro Neto, J. Leist, A. K. Geim, L. A. Ponomarenko, and K. S. Novoselov, *Nano Letters* **12**, 1707 (2012).
- [29] We acknowledge that the 7L device exhibits two switching events: the first is the switching of the junction and the second is likely due to one of the NbSe₂ flakes being driven out of its superconducting state due to the application of a large (~ 1 mA) bias current.
- [30] H. Courtois, M. Meschke, J. T. Peltonen, and J. P. Pekola, *Physical Review Letters* **101**, 1 (2008).
- [31] W. C. Stewart, *Applied Physics Letters* **12**, 277 (1968).
- [32] D. E. McCumber, *Journal of Applied Physics* **39**, 3113 (1968).
- [33] V. Ambegaokar and A. Baratoff, *Physical Review Letters* **11**, 104 (1963).
- [34] F. Gross, B. S. Chandrasekhar, D. Einzel, K. Andres, P. J. Hirschfeld, H. R. Ott, J. Beuers, Z. Fisk, and J. L. Smith, *Zeitschrift für Physik B Condensed Matter* **64**, 175 (1986).
- [35] I. Kulik and A. Omel'yanchuk, *Journal of Experimental and Theoretical Physics Letters* **21**, 96 (1975).
- [36] W. Haberkorn, H. Knauer, and J. Richter, *Physica Status Solidi (a)* **47**, K161 (1978).
- [37] A. A. Golubov, M. Y. Kupriyanov, and E. Il'ichev, *Reviews of Modern Physics* **76**, 411 (2004).
- [38] A. Golubov and M. Y. Kupriyanov, *Soviet Physics JETP* **69**, 805 (1989).
- [39] A. A. Golubov, M. A. Gurvich, M. Y. Kupriyanov, and S. V. Polonskii, *Journal of Experimental and Theoretical Physics Letters* **76**, 915 (1993).
- [40] A. A. Golubov, E. P. Houwman, J. G. Gijsbertsen, V. M. Krasnov, J. Flokstra, H. Rogalla, and M. Y. Kupriyanov, *Physical Review B* **51**, 1073 (1995).
- [41] Y. C. Chen, M. P. A. Fisher, and A. J. Leggett, *Journal of Applied Physics* **64**, 3119 (1988).
- [42] C. Zhang, C. Gong, Y. Nie, K.-A. Min, C. Liang, Y. J. Oh, H. Zhang, W. Wang, S. Hong, L. Colombo, R. M. Wallace, and K. Cho, *2D Materials* **4**, 015026 (2017).
- [43] J. Guan, H.-J. Chuang, Z. Zhou, and D. Tománek, *ACS Nano* **11**, 3904 (2017).
- [44] Y. Sata, R. Moriya, S. Masubuchi, K. Watanabe, T. Taniguchi, and T. Machida, *Japanese Journal of Applied Physics* **56**, 04CK09 (2017).
- [45] A. Anferov, F. Wan, S. P. Harvey, J. Simon, and D. I. Schuster, (2024), arXiv:2411.11170.
- [46] S. Liu, Y. Liu, L. Holtzman, B. Li, M. Holbrook, J. Pack, T. Taniguchi, K. Watanabe, C. R. Dean, A. N. Pasupathy, K. Barkmak, D. A. Rhodes, and J. Hone, *ACS Nano* **17**, 16587 (2023).
- [47] R. Kenaz, S. Ghosh, P. Ramachandran, K. Watanabe, T. Taniguchi, H. Steinberg, and R. Rapaport, *ACS Nano* **17**, 9188 (2023), arXiv:2211.07437.
- [48] Y. Li, Y. Rao, K. F. Mak, Y. You, S. Wang, C. R. Dean, and T. F. Heinz, *Nano Letters* **13**, 3329 (2013).